



# Elevation change of the Greenland Ice Sheet and its peripheral glaciers: 1992–2023

Johan Nilsson<sup>1,2</sup> and Alex S. Gardner<sup>2</sup>

<sup>1</sup>Department of Earth Science, Uppsala University, Uppsala, Sweden

<sup>2</sup>Jet Propulsion Laboratory, California Institute of Technology, Pasadena, CA 91109, USA

**Correspondence:** Johan Nilsson (johan.n.nilsson@geo.uu.se)

Received: 22 July 2024 – Discussion started: 21 October 2024

Revised: 3 December 2025 – Accepted: 4 January 2026 – Published: 5 March 2026

**Abstract.** The integration of data from multiple satellite altimetry missions, each offering unique observational characteristics, has enabled us to discern both short-term variability and long-term climate trends affecting Greenland’s peripheral glaciers and the Greenland Ice Sheet (GrIS). Our methodology, informed by lessons learned from analogous efforts in Antarctica and by improved incorporation of external velocity and elevation data to reduce bias in elevation-change estimates, ensures the consistency and reliability of the derived dataset. An additional enhancement of this product is the inclusion of a digital elevation model, which facilitates the analysis of changes in absolute elevation. The dataset covers the years 1992–2023 and is publicly available as part of NASA’s Making Earth System Data Records for Use in Research Environments (MEaSUREs) Inter-Mission Time Series of Land Ice Velocity and Elevation (ITS\_LIVE) project (<https://doi.org/10.5067/ICFVI7DKHZJV>, Nilsson et al., 2026). Our analysis reveals significant patterns of mass loss across the GrIS. We find that the ice sheet and peripheral glaciers experienced average mass losses of  $-160 \pm 17$  and  $-23 \pm 5 \text{ Gt a}^{-1}$ , respectively, over the 1992–2023 period, with notable temporal variations. Specifically, the early years of the record exhibit a positive mass balance, likely driven by anomalously positive surface mass balance. However, this trend reverses in later years, with a pronounced increase in mass-loss rates that highlights the accelerating impact of climate change on ice-sheet dynamics and surface mass balance. Moreover, our analysis underscores the importance of considering peripheral glaciers alongside the continental ice sheet when assessing overall mass trends. By incorporating data from peripheral glaciers, we provide a more comprehensive understanding of Greenland’s total contributions to global sea-level rise. Our findings reveal not only the magnitude of mass loss but also its evolution through time, emphasizing the need for continued monitoring and research to better understand the impacts of climate change on Earth’s cryosphere.

## 1 Introduction

The Greenland Ice Sheet (GrIS) is the second largest reservoir of freshwater, after the Antarctic Ice Sheet (AIS), and has the potential to raise global sea levels by approximately seven meters if completely melted (Houghton, 2004). Currently, it is the one of the largest contributor to eustatic sea level rise, surpassing the Antarctic Ice Sheet (Otosaka et al., 2023) and comparable to the rest of the world’s glaciers. It is projected that by the end of the century, the GrIS will contribute over 30 cm to global sea levels under high-

emission scenarios (Hugonnet et al., 2021). Over the past three decades, starting from the onset of the satellite altimetry era in 1992, it is estimated that the GrIS lost nearly  $3.8 \times 10^{12} \text{ t}$  of ice, resulting in a global sea level rise of approximately 11 mm (The IMBIE team, 2018). Satellite altimetry plays a crucial role in studying changes in the cryosphere at continental scale. The remoteness and vast expanse of the world’s ice sheets necessitate long-term space-based remote sensing to distinguish short-term variability from long-term climate trends. The satellite altimetry record for cryosphere studies began in the early 1992 and continues to the present

day, incorporating several altimetry missions with varying characteristics (e.g., radar and laser altimeters).

Generating continuous time series of elevation change from satellite altimetry is a complex task with several challenging processing steps. These steps include geophysical corrections, waveform retracking, static topography removal, scattering regime corrections, cross-calibration, and more. In this study, we present a new dataset that incorporates all the corrections, enabling the generation of a continuous elevation change dataset for Greenland that spans the period from 1992 to 2023. Using the methodology developed in an earlier study of Antarctic Ice Sheet elevation change (Nilsson et al., 2022), we synthesize data from six different satellite altimetry missions collected over Greenland, comprising of both radar and laser altimeters. Additional attention was devoted to refining the remove–restore technique employed in the previous Antarctic study, thereby enhancing the recovery of spatially variable mass signals in the outlet and peripheral regions of the ice sheet. Moreover, a digital elevation model (DEM), derived from altimetry and external elevation data, is provided. In contrast to our earlier work, this DEM facilitates the assessment of changes in absolute topography that are fully vertically aligned with the elevation-change dataset over the 1992–2023 period. The resulting dataset has undergone comprehensive validation using independent, unbiased airborne laser altimetry data. This effort is part of the ITS\_LIVE project (<https://its-live.jpl.nasa.gov/>, last access: 11 February 2026), which has been developed over the last few years to generate synthesized and continuous elevation, velocity and ice extent records for both the Greenland and Antarctic Ice Sheets. ITS\_LIVE has already published a longer record of elevation change for the Antarctic Ice Sheet, covering the period from 1985 to 2020. The lessons learned and methodology from the processing of the Antarctic data have been applied to this new product for Greenland.

This study represents the most complete synthesis of satellite altimetry data to date, covering the period from 1992 to 2023. Notably, it includes not only the continental ice sheet but also three decades of change of Greenland's peripheral glaciers for the first time. This record was used in combination with two firn models to estimate that Greenland (continental ice sheet plus periphery glaciers) lost a total of  $5120 \pm 544$  Gt of ice over the 1992–2023 period with large inter-decadal variability. The ice sheet and peripheral glaciers had a mass budget of  $+51 \pm 68$  Gt a<sup>-1</sup> in the first decade of the record, a budget of  $-303 \pm 48$  Gt a<sup>-1</sup> in the second decade, and a rate of  $-124 \pm 39$  Gt a<sup>-1</sup> in that last decade.

## 2 Data and coverage

In this study we utilized a total of six missions to obtain a 32-year long time series of elevation changes for the GrIS and its peripheral glaciers spanning the period from 1992

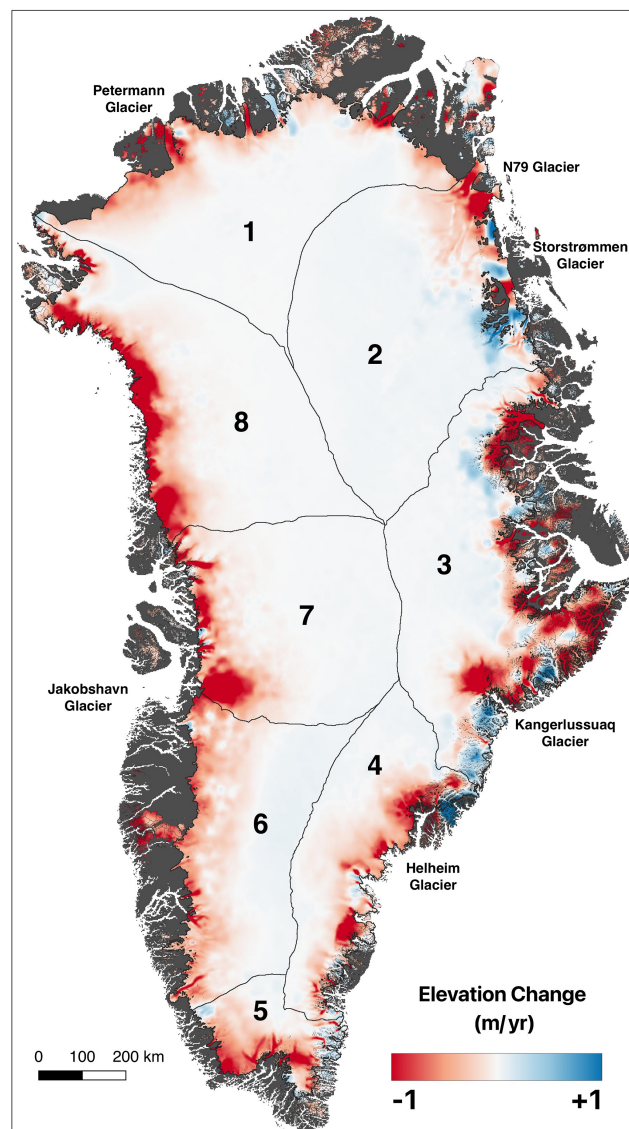


**Figure 1.** Elevation change of the Greenland Ice Sheet and glacier from 1992 to 2023. Drainage basins 1–8 (Zwally et al., 2012) shown in black with labelling of large outlet glaciers.

to 2023. The missions encompassed both radar and laser altimeters that operated during different overlapping time intervals: the European Remote Sensing (ERS) satellites ERS-1 (1992–1996) and ERS-2 (1995–2003), the Environmental Satellite (Envisat) (2003–2012), the Ice, Cloud, and land Elevation Satellites (ICESat) (2003–2009) and ICESat-2 (2018–Present), and CryoSat-2 (2010–Present). Additional information regarding the different missions can be found in Table 1. The methodology for geophysical corrections and data editing for each mission follows the same approach as described in the reference paper of Nilsson et al. (2022), with a few minor modifications that we detail here. For Envisat, we utilized the entire period of operation. This differs from our pre-

vious study, which only used Envisat data through to the orbit change that occurred in late October of 2010. Including the additional 17 months of data enabled better overlap with CryoSat-2. Additionally, we employed the latest fully reprocessed Envisat data, specifically the “RA-2 Level 2 products: the Geophysical Data Record (GDR) version 3.0” (Anon, 2018). For CryoSat-2 we use the updated L1b Baseline-E for both the Low-Resolution Mode (LRM) and the Interferometric Synthetic Aperture Radar (SARIn) modes (available at <https://science-pds.cryosat.esa.int>, last access: 29 November 2025). For ICESat we apply Laser-2/Laser-3 biases based on the recommendation provided in Borsa et al. (2019), this was not done in Nilsson et al. (2022). For ICESat-2 we utilized release-006 of the ATL06 (Smith et al., 2023). For ERS-1/2 we used the REAPER product (REprocessing of Altimeter Products for ERS) from Brockley et al. (2017). Otherwise we use the same data and follow all of the processing steps described in Nilsson et al. (2022) that we summarize in the Methods.

To convert from volume change to mass change we utilized two different Firn Densification Models (FDM) to account for changes in the Firn Air Content (FAC) that result in changes in ice volume without any corresponding change in mass. We use the Glacier Energy and Mass Balance FDM (GEMB) version 1.3 (Gardner et al., 2023) and the Goddard Space Flight Center FDM version 1.2.1 (GSFC) (Medley et al., 2022). Both products contain model results for the continental ice sheet and peripheral glaciers. The modelled FAC was interpolated in space and time from their native output to our 1920 m resolution and monthly temporal sampling using simple linear interpolation through the end of 2023. To compute mass change, FAC volume changes were subtracted from glacier volume changes to determine the ice equivalent volume change. The ice equivalent volume change was then multiplied by the density of ice ( $917 \text{ kg m}^{-3}$ ) to determine mass change from the two models, and the final mass change estimate is obtained by taking the mean of two estimates.

To delineate the continental ice sheet we use a mask dataset provided by Frank Paul (Bolch et al., 2013) and for its drainage basins we used outlines from Zwally et al. (2012). For peripheral glaciers, we used Region 5 of the “Randolph Glacier Inventory 6.0” (RGI) (RGI Consortium, 2017), including only the weakly connected and unconnected glaciers (CL1 and CL0). The outlines are available in Fig. S6 in the Supplement.

### 3 Methods

To derive continuous long-term elevation change estimates for the GrIS we closely follow Nilsson et al. (2022) with some minor updates and improvements. The final gridded dataset has a nominal spatial resolution of 1920 m, reflecting the resolution achieved through the combination of the “stacking” procedure and subsequent interpolation. How-

ever, individual corrections applied to the dataset are mostly performed at the point level, with search radii chosen to match the specific requirements of each correction, as detailed in the steps below.

#### 3.1 Reading and editing of altimetry data

Reading and editing of the altimetry data, and application of the standard corrections (dry and wet troposphere correction, ionosphere correction, load tide, pole tide and solid earth tide) followed the same procedure as Nilsson et al. (2022). For ICESat we did not apply an inter-campaign correction following our previous Antarctic study, but we do apply a 3.1 cm bias between ICESat’s Laser 2 and Laser 3 as suggested by Borsa et al. (2019).

#### 3.2 Slope correction of pulse-limited radar altimetry data

Over an inclined surface the radar return does not originate from nadir, but rather from the point-of-closest-approach (POCA). Assuming that the return comes from nadir leads to both incorrect estimate of elevation and the position of the return (Brenner et al., 1983). Due to the large size of the ground footprint of pulse-limited radars ( $\sim 16 \text{ km}$  in diameter – beam-limited) the surface return can originate from anywhere inside this region. To mitigate this error a correction is needed based on the shape of the topography within the pulse-limited footprint. There are several types of corrections available (see Bamber, 1994). In this study we employ the relocation method (Nilsson et al., 2016; Roemer et al., 2007; Schröder et al., 2017) to correct both the position and the elevation each echo (on a point by point basis). This was done by using the slope and aspect estimated from the GIMP digital elevation model (Howat et al., 2014) down sampled (by averaging) to 2 km mimicking the size of the pulse-limited footprint. 2 km has been shown to provide the most accurate correction when compared to airborne laser data (Levinsen et al., 2016). This correction is not needed for laser altimetry (ICESat and ICESat-2) and for CryoSat-2 SARIn mode because of the small footprint size and the interferometric capabilities, respectively.

#### 3.3 Separation of static and time variable topography

To resolve time variable changes in surface elevation the underlying time-averaged topography needs to be removed to create a time varying point-cloud. Following Nilsson et al. (2022), we separate static and time variable topography by removing a biquadratic surface model from the point data. Time variable height was computed on a  $500 \times 500 \text{ m}$  grid with a 1000 m search radius for CryoSat-2 and a 500 m search radius for all other missions. In contrast to our Antarctic product, we did not separate ascending and descending tracks when separating separate static and time variable topography. This is because over Greenland we did not detect

**Table 1.** Overview of the key satellite mission parameters for each mission and operational mode. For ERS-1, ERS-2, and Envisat, the table reports parameters corresponding to the nominal (non-geodetic) repeat cycles, which represented the primary operational mode during the respective missions. Periods when the satellites operated in geodetic, drifting, or campaign-specific orbits: ERS-1 flew a dedicated geodetic orbit during 1992–1993, ERS-2 had geodetic-mode operations mainly during 1995–1996 and select short intervals later in the mission, and Envisat’s orbit drifted from 2010–2012 to extend coverage beyond the nominal 35 d repeat cycle.

Mission	Footprint Size	Along-Track Sampling	Repeat Cycle	Latitude Coverage
ERS-1	~ 2 km (pulse-limited)	~ 335 m	35 d repeat (non-geodetic)	±81.5°
ERS-2	~ 2 km (pulse-limited)	~ 335 m	35 d repeat (non-geodetic)	±81.5°
Envisat	~ 2 km (pulse-limited)	~ 370 m	35 d repeat (non-geodetic)	±81.5°
ICESat	~ 70 m (beam-limited)	~ 150–170 m	Campaign-based (~ 12–55 d per campaign)	±86.0°
CryoSat-2 LRM	~ 1.6–1.7 km (pulse-limited)	~ 300 m	369 d long-repeat orbit (~ 30 d sub-cycle)	±88.0°
CryoSat-2 SARIn	~ 300 m × 1.5–1.7 km (doppler/delay)	~ 300 m	369 d repeat orbit (~ 30 d sub-cycle)	±88.0°
ICESat-2 ATL06	~ 17 m (beam-limited)	20 m segment spacing	91 d repeat orbit	±88.0°

any ascending/descending biases of consequence, which is in agreement with Schröder et al. (2019). The static topography output from the separation procedure, which corresponds to the intercept of the biquadratic surface fit, was used to generate a multi-mission elevation model. Because the different elevation estimates are centered and trend-corrected to their respective mission midpoints, adjustments for offsets and spatial gradients can be performed using a bilinear plane surface, along with offset and trend terms (like the cross-calibration procedure in Sect. 3.7). This procedure enables the alignment of all mission elevations to the reference year 2014. The alignment was conducted at 1 km resolution using a 1 km search radius. The resulting mean elevation, corresponding to the intercept, was then differenced with ArcticDEM (Porter et al., 2023) to improve coverage in areas of low spatial density, consistent with the approach described in Winstrup et al. (2024). The residuals were subsequently gridded using a median operator applied to the 25 nearest points, which corresponds to an approximate 5 km search radius determined from covariance analysis. Prior to gridding, residuals exceeding 50 m were removed. Finally, ArcticDEM was added back to the interpolated residuals to produce an updated digital elevation model centered on 2014.

### 3.4 Scattering correction of radar altimetry data

Most radar altimeters operate in Ku band (13.6 GHz) that is sensitive to radar penetration into snow and ice (Arthern et al., 2001). This sensitivity introduces errors into in

the retrieved elevation, causing changes in both the measured trend and the seasonal variability (Davis and Ferguson, 2004; Khvorostovsky, 2012; Nilsson et al., 2015; Wingham et al., 1998). To mitigate this effect, a local regression is performed between the backscattered power, the leading edge and the trailing edge slope with height change elevation and subtracted from each individual elevation data point (Flament and Rémy, 2012; Nilsson et al., 2022; Paolo et al., 2016; Simonsen and Sørensen, 2017; Zwally et al., 2005). Here, each point dataset is divided into  $1 \times 1$  km spatial bins, and the regression is performed to the data within each bin. Compared to our previous work a modification was done to remove the mean for each waveform parameter inside the bin instead of differencing, a similar approach to Flament and Rémy (2012). Tests around the “The North Greenland Eemian Ice Drilling” (NEEM) station showed improved trends and seasonality when removing the mean, relative to differencing. Hence, care should be taken when selecting this type of operation as it might be dependent on the magnitude of penetration depth and the differences in scattering characteristics for the Greenland and Antarctic ice sheets (e.g. wet versus dry). It was noticed in the previous application of the scattering correction algorithm for our study in Antarctica that issues could arise when no-data values were present in the individual waveform parameters, providing erroneous solutions. To reduce this issue a simple spatio-temporal nearest neighbour interpolation steps was added to fill no-data values for each waveform parameter before the inversion.

### 3.5 Stacking of multi-mission altimetry data to a regular spatio-temporal grid

To create monthly time series of elevation change spatio-temporal binning or “stacking” was employed. Here, we stacked/binning the point-data onto a monthly  $1920 \times 1920$  m regular grid  $(t, x, y)$  using a constant search radius of 10 km around each node. This is one of the updates from our previous version of the processing pipeline, which applied the stacking in the cross-calibration step. Here stacking and cross-calibration were separated to provide simplified and efficient re-processing of data. Another improvement in the stacking step was to use an exponential spatio-temporal kernel to generate monthly estimates of elevation change. Here, a 3-month window of data was used to estimate the monthly weighted averages within the 10 km search radius using a correlation length of 1920 m that is consistent with the spatial resolution of the grid and the resolution of the pulse limited radar missions. This procedure introduces light interpolation and smoothing to the data, benefiting start and endpoints. This also provides improved overlap between missions, which are needed for mission cross-calibration. To reduce noise in monthly estimates, each time series was filtered before stacking by fitting a third order polynomial plus seasonal model to the data and rejecting data falling outside  $10\sigma$  and  $\pm 10$  m of the residuals. Further, inside each 3-month window we rejected data falling outside  $10\sigma$ . Sigma-editing was performed using the scaled “Median Absolute Deviation” (MAD) as previously used in Nilsson et al. (2022).

### 3.6 Normalization of seasonal amplitudes

It is well documented that radar penetration influences the magnitude of the retrieved seasonal signal observed by radar altimeters (Davis and Ferguson, 2004; Nilsson et al., 2015; Wingham et al., 1998; Khvorostovsky, 2012). The degree and nature of radar penetration is mission dependent. This causes varying observed seasonal amplitudes between missions. A large part of this inter-mission seasonal amplitude variability is corrected for by the scattering correction (Sect. 3.4) but not all. This can be observed in the products of Schröder et al. (2019) and Nilsson et al. (2022). To normalize seasonal amplitudes between mission we apply the same method as used in Antarctic study. Here, a reference mission is used to create a seasonal correction based on the ratio of between the reference mission and target mission for each binned time series. Once this correction is estimated it is then removed from the target mission aligning its overall seasonal amplitude with the reference. CryoSat-2 was selected as reference mission due to previous experience over Antarctica. The correction was only applied to the radar altimetry (excluding CryoSat-2) data and not to ICESat or ICESat-2. The correction was estimated for each grid node on the stacked data by first removing a 3rd order polynomial and then fitting a seasonal model to each time series. Using the estimated seasonal model, a

scaled version based on the amplitude, was created and removed from each radar time series. In the last step the 3rd order polynomial was added back. Currently, there is an ongoing efforts to reduce or mitigate issues relating to artificial trends and seasonality in the retracking stage using convolutional neural networks (Helm et al., 2024).

### 3.7 Cross-calibration of multi-mission altimetry data

The different stacked altimetry time series need to be cross calibrated at each grid node to produce an aligned record. This is achieved using an two-step processed outlined in Nilsson et al. (2022) which consists of fitting a polynomial of variable order (order ranging from 1 to 5) with an added annual and semi-annual seasonal model in combination with an overlap bias term. The model order is determined using the “Bayesian information criterion” as previously done. The coefficients for this model are then solved for using iterative least-squares with a maximum of five iterations in combination with a  $10\sigma$  and  $\pm 10$  m filter. Due to variable data coverage, mission biases cannot be determined everywhere. We therefore interpolated the bias to each node and remove it from each mission time series. To account for any nonlinearities not captured by the selected model, a secondary calibration offset is generated by computing the median difference of the model residuals for each overlapping period for each mission. This residual offset after the initial correction is then interpolated and removed in the same manner as before. One should note that to reduce the number of overlaps, the different missions (and modes) are first grouped after the initial least squares adjustment, and the offsets computed on the grouped overlaps. Missions are grouped as follows: ERS-1 (Ocean/Ice-mode), ERS-2 (Ocean/Ice mode), Envisat with ICESat, CryoSat-2 (SARIn/LRM-mode) and ICESat-2 creating a total of five groups (i.e., five overlaps). For Greenland we found that there was no need to provide an external rate comparison of cross-calibration offsets to the ICESat-2 mission as done in Nilsson et al. (2022). The residual cross-calibration algorithm could then be simplified to only use Solution 1 in Nilsson et al. (2022) where the offset is simply computed by differencing the median values for each overlapping part of the time series for each group.

### 3.8 Interpolation and merging of multi-mission time series

Here, the merging and the interpolation of the stacked 1920 m resolution data is performed in the same step using the individual measurement error as the weighting in the interpolation procedure. We update the optimum interpolation routine relative to Nilsson et al. (2022). In our previous study the selected background fields, based on velocity and hypsometry, were applied locally using the closest data in horizontal distance. Our analysis showed that the local approach was not robust and that using a background model

based on data from a larger region ( $\sim 150$  km) provided improved results. Further modifications to the model were to remove the log-transform applied to the velocity data. To provide full coverage at each node and to reduce variability in the velocity estimates both the velocity and DEM were averaged to 1920 m resolution. Then velocity and hypsometry are static and do not change over time following the approach Hurkmans et al. (2012). They were binned in 100 m elevation bands at each grid node using data within 150 km radius and regressed against the elevation change difference for that specific month.

$$dh = c_0 + c_1 v + c_2 h_{\text{DEM}} \quad (1)$$

were,  $v$  is the velocity and  $h_{\text{DEM}}$  is the hypsometry from the digital elevation model. Ice sheet dynamics are best captured by changes in surface velocity. However, radar altimetry is unable to measure changes in areas of complex terrain. Studying the relationship between elevation change and velocity magnitude on a continental and regional wide basis we find relatively linear relationship up to roughly  $300\text{--}500 \text{ m a}^{-1}$ , after which the correlation decreases rapidly. Examples of the relationship between elevation change, velocity, and hypsometry can be seen in Fig. S7. This decrease in correlation is most likely related to the inability of the altimeter to measure areas of fast flow that are most often located in areas of complex topography, like outlet glaciers. Because of this, we assume that the linear relationship for low velocities can be extrapolated to areas of higher velocities. To capture the relationship between velocity magnitude and elevation change in the model we weight the solution using the inverse squared of the velocity ( $w = 1/v^2$ ) in the multivariate regression. The weight is used to focus the fit on the velocity range that is more stable than. No weighting regarding elevation ( $h_{\text{DEM}}$ ) was done but could be investigate and included in future solutions. We have provided examples of these relationships in the Supplement (Fig. S7). For each node we select data within a 150 km radius or the 3000 closest points (if less than 3000 points are available), the coefficients of the model are solved for and subtracted from the closest 49 points for that node to reduce the computational burden. The residuals of these 49 points compared to the model are used to predict the value at the grid node using least-squares collocation (optimum interpolation). A second order Gauss-Markov model is used to model the covariance assuming a 20 km correlation length. To reduce “trackiness” in the gridded spatial fields a variance of  $1 \text{ cm}^2$  to the off-diagonal elements of the covariance matrix (similar to Paolo et al., 2023). Once the value at the grid node has been estimated from the residual data the background model is added back to restore the signal of each monthly spatial field. This is referred to as the remove and restore technique and has been widely used in geodesy for decades (Moritz, 1978). Before the interpolation stage a simple spatial filtering is performed. Each monthly spatial field is divided into 100 km bins and inside each bin a biquadratic surface model is fit to the data. This surface fitting is done

to account for any spatial gradients in the elevation change data, which exists in each monthly spatial field. The residuals to this model fit are used to identify and reject outliers using the “inter-quantile range” (IQR) using the 25th (Q1) and 75th (Q3) percentile: (Lower bound =  $Q1 - 1.5 \times \text{IQR}$ , Upper bound =  $Q3 + 1.5 \times \text{IQR}$  and  $\text{IQR} = Q3 - Q1$ ) inside each bin to reduce any gross outliers.

### 3.9 Post filtering and smoothing of product

The final stage of processing involves filtering each individual stacked and interpolated time series (only in time) to eliminate and replace outliers. Initially, a LOWESS algorithm (Cleveland, 1979) is employed to estimate the time series trend, and outliers are identified and removed using a  $10\sigma$  edit based on the median absolute deviation (MAD) of the residuals with respect to the temporal trend. Subsequently, the residuals to the fit are further refined using a moving 12-month window of an interquartile range (IQR) filter to eliminate any remaining monthly outliers (identical to the filter in Sect. 3.8). Rejected epochs are then filled and slightly smoothed by convolving the time series with a Gaussian kernel having a correlation length of three months and a filter length of nine months. Any unfilled regions resulting from these processes are spatially filled using a Gaussian kernel with a correlation length of roughly 20 km (in line with the correlation length used in the interpolation step) with a radius of 30 km for each monthly spatial field. Finally, a difference operator is applied to identify and remove any month-to-month differences exceeding 50 m. If such differences are detected, the entire time series for that node is rejected and subsequently re-interpolated spatially using the surrounding data for each month.

## 4 Error propagation and validation

Airborne laser altimetry has been collected over the GrIS since the early 1990’s. More than 88-million-point elevation measurements have been collected by the Airborne Topographic Mapper (ATM) instrument (MacGregor et al., 2021) carried on multiple missions over Greenland starting in 1993 until the end of Operation IceBridge (OIB) in 2019. This makes it a vital source of validation data for space-borne altimeters. We validate our product against ATM data to estimate the uncertainty of our derived surface elevations. For each mission point-to-point elevation difference (altimetry minus airborne) are computed from data within a search radius of 50 m and a three-month window. The three-month window was selected to obtain enough samples for the older mission. The selection of the temporal window size had little effect on the overall statistics. Statistics are sensitive to the selection of the horizontal search radius and is a trade-off between the number of samples and decreased precision. Our selection of a 50 m search radius is based on previous work (Gray et al., 2017; Nilsson et al., 2016). Elevation differences

**Table 2.** Estimates of elevation error for different missions and modes through comparison with airborne measurements. Elevations within 50 m of each other were selected with a maximum time difference of three months. Tabulated below is the estimated noise level ( $\sigma_i$ ) of each dataset and its corresponding error as a function of surface slope ( $\sigma_{\text{slope}}$ ). The errors were generated by computing the standard deviation of the difference as a function of surface slope at  $0.05^\circ$  intervals from  $0\text{--}0.5^\circ$ .

Mission	$\sigma_{\text{noise}}$ (m)	$\sigma_{\text{slope}}$ (m degree <sup>-2</sup> )	Count
ERS-1 (Ocean)	0.24	21.32	678
ERS-1 (Ice)	0.37	30.21	6963
ERS-2 (Ocean)	0.06	19.91	540
ERS-2 (Ice)	0.41	29.85	35 734
Envisat	0.15	34.85	62 320
ICESat	0.11	0.71	7192
Cryosat-2 (LRM)	0.12	23.70	25 587
CryoSat-2 (SARIn)	0.34	1.26	36 346
ICESat-2	0.07	0.43	123 951

were then binned by surface slope derived from the GIMP digital elevation model (Howat et al., 2014) at intervals of  $0.05^\circ$  from  $0$  to  $0.8^\circ$  (see Fig. 2). An error model was fit following (Schröder et al., 2019; Smith et al., 2020) to obtain the overall noise level of each mission and their sensitivity to surface slope. The error model was taken to be:

$$\sigma_i = \sigma_{\text{noise}} + \sigma_{\text{slope}} \alpha^2 \quad (2)$$

where  $\sigma_i$  is the binned standard deviation,  $\sigma_{\text{noise}}$  is the estimated noise level at zero slope,  $\sigma_{\text{slope}}$  is the slope dependent error (sensitivity) and  $\alpha$  is the surface slope in degrees. The error model was fit from  $0$  to  $0.5^\circ$  surface slope to obtain a good fit: bins with slopes  $> 0.5^\circ$  have higher variability (Fig. 2) due to lower data counts. Model fit results are summarized for each mission in Table 2.

The estimated noise level is used as a measure of the systematic error of each mission or mode. The random error is estimated from the variability of the elevation change data for each monthly estimate in the spatio-temporal stacking procedure. To estimate the total error for each monthly estimate of elevation change the two error components can be combined using root-sum-squares (RSS) after scaling the random error using an appropriate correlation length. The random error is then used as input in the gridding procedure as the measurement error and added to the diagonal elements of the covariance matrix. The final elevation change product includes monthly fields of both random and systematic error. This allows the user to derive an independent error budget if needed (i.e., to account spatial autocorrelation in the random error).

To estimate the accuracy of long-term elevation change rates, and to maximizing spatial coverage, elevation change rates were estimated from the ATM data over the time period 1993–2019, following the approach of (McMillan et al., 2016; Nilsson et al., 2022; Wouters et al., 2015). Elevation change estimates were computed by fitting a linear model

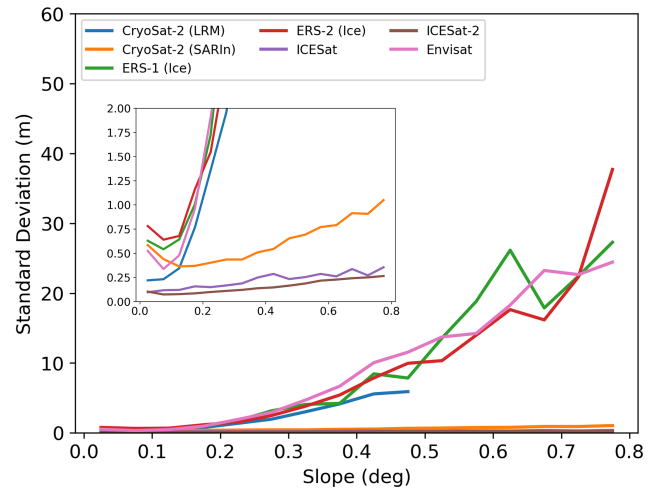


**Figure 2.** Mission dependent elevation error as a function of surface slope. The figure highlights the recent improvements in ice sheet altimetry with the introduction of both laser (ICESat and ICESat-2) and interferometric synthetic aperture radar (CryoSat-2 SARIn mode). See Table 2 for derived parameters.

to the elevation data inside a search radius of 175 m around each ATM reference track location. The data was centred to 2006, and the solution was discarded if the estimated rate was larger than  $20 \text{ m a}^{-1}$ , if the number of points in the solution was less than ten, or if the maximum time difference was less than five years. The derived rates were then averaged to the same spatial resolution as our height change product (1920 m) and subsequently differenced with the altimetry (altimetry minus airborne). The results of the elevation change rate validation are presented in Fig. 3. To validate the digital elevation model generated for this product, the same procedure described above was applied, with the central reference year set to 2014 rather than 2006. The intercept derived from the ATM data was then compared with the corresponding DEM values using the same methodology.

To estimate errors in rates of mass change for different time intervals we followed the approach of Nilsson et al. (2022). For each region of interest (drainage basin, peripheral or continental estimates) the mass change rate error was computed by taking the mean random and systematic elevation errors for each time series inside the specified time interval. The random error was then divided by the square root of the number of un-correlated spatial bins estimated as:

$$N = A_{\text{ROI}} / \pi r^2 \quad (3)$$

where  $A_{\text{ROI}}$  is the total area of the region of interest (ROI) and  $r$  is the correlation length of the data. In this study we set  $r = 40 \text{ km}$ . The correlation lengths were selected from a covariance analysis of elevation changes for each monthly spatial field for the two regions. The systematic and random error are then added in quadrature and the corresponding mass

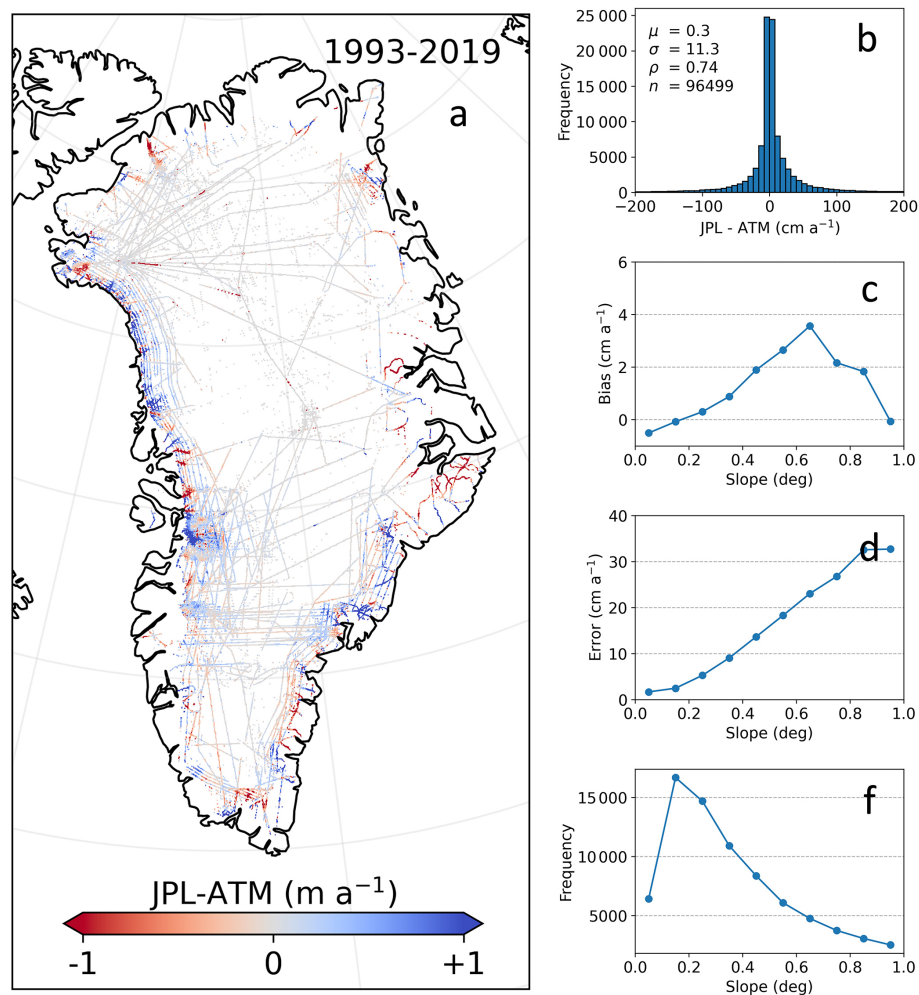


**Figure 3.** (Left) Difference in elevation change rates over the Greenland Ice Sheet between our synthesis height change product and ATM airborne laser altimetry covering the period 1993–2019 (a). (Right) Corresponding statistics and surface slope dependencies of the differences.  $\sim 100\,000$  points have been used in the analysis to generate long-term statistics covering a diverse range of slopes and surface conditions. An overall difference of  $0.30 \pm 11\text{ cm a}^{-1}$  (b) is found over the entire region with an error of  $\sim 2.0\text{ cm a}^{-1}$  for the flat regions increasing to  $\sim 35\text{ cm a}^{-1}$  in the high-slope regions close to the margins of the ice sheet (c, d). Further, the effect of the background model is evident in the bias (c, f) where a decrease in bias can be observed in the high-slope areas of the ice sheet.

rate ( $\varepsilon_{\text{rate}}^2$ ) error for each time interval is computed by dividing by the desired time span.

Estimating FAC errors is an active area of research and not within the scope of this study. Instead, we take the difference in FAC change between the two models as the measure of error. The error in the derived firn-rate for each time interval is then estimated as the RMSE (including bias and variance) of the volume difference of the FDM models divided by the time span. The variance in the RMSE computation was scaled by the number of un-correlated bins, as done previously, using a correlation length of 200 km defined from a covariance analysis. To derive mass change errors in gigatons per year we added the volume change error and FAC error in quadrature then multiplied by the density of ice.

## 5 Results

Our estimates of elevation change (Figs. 1 and 4) are in line with previous studies (Khan et al., 2022; Otosaka et al., 2023) for areas of large change, such as Jakobshavn, Helheim, Kangerlugssuaq and Storstrømmen glaciers. However, by incorporating the background model, guided by velocity and hypsometry, we have achieved improved characterization of the magnitude of the pronounced dynamic thinning, such as Jakobshavn, Helheim, and Kangerlussuaq glaciers. Here, one can clearly see the slowdown of Jakobshavn in the 2017–2021 period due to ocean cooling (Khazendar et al., 2019). This is noteworthy considering that many previous altimetry-derived studies have relied on more classical interpolation algorithms (e.g., kriging, Inverse distance weighted

(IDW) interpolation etc.), resulting in the spatial smoothing of these highly localized signals. The applied background model addresses spatial sampling biases inherent to radar satellite altimeters, which tend to under-sample troughs and valleys. By comparing the long-term trend differences between the velocity and elevation guided solution (i.e., using a background model) versus ordinary kriging/optimum interpolation, we find a difference here of  $-40 \text{ km}^3 \text{ a}^{-1}$  with the background model approach providing more negative results. Further, validation of the effectiveness of this technique is demonstrated in Fig. S1 of the Supplement, where a comparison with ATM-derived rates was conducted. Notably, the selected background model exhibited significantly reduced overall bias when analyzing steeper slopes (slopes  $> 0.5^\circ$ ).

The accuracy, or noise levels, of the independent missions vary depending on their age. Older missions like the ERS exhibit an overall ice sheet-wide accuracy of approximately 40 cm (Fig. 2 and Table 2). In contrast, the more recent missions demonstrate improved accuracy ranging from 7 to 15 cm, except for CryoSat-2 SARIn, which has an accuracy of around 35 cm due to its operational focus on areas with complex topography (Fig. 2 and Table 2). Most notably, difference can be observed between radar and laser derived surface elevations where laser outperforms radar over all slope intervals. It should however be noted that CryoSat-2 SARIn mode provides significant improvements compared to traditional pulse-limited altimetry. Over the slope range of  $0.1\text{--}0.8^\circ$  CryoSat-2 show a higher slope dependency with an error ranging from 35 to 100 cm while ICESat and ICESat-2 show an error ranging from 10 to 20 cm. The impact of mission quality can also be seen in timeseries error bars shown in Fig. 5, most notably the reduction in error after the launch of ICESat-2 in 2018.

Analyzing the overall quality of our product, in the form of long-term elevation changes rates, we find a difference of  $0.3 \pm 11.3 \text{ mm a}^{-1}$  based on a comparison to  $\sim 100\,000$  ATM samples plus an additional slope dependent error of  $1\text{--}35 \text{ cm a}^{-1}$  (Fig. 3). Error is roughly 50% lower for our “background” interpolation algorithm compared to ordinary optimal interpolation. These results vary regionally and as observed in Fig. 3, areas of rapid change such as the GrIS outlet glacier discrepancies still exist. For the generated DEM we find an overall absolute error of  $1.9 \pm 4.6 \text{ m}$  when comparing to the ATM derived elevation generated in the same procedure. Figure S6 presents a hillshade rendering of the generated DEM. We also compare our product to PROMDEM over the 2019–2023 period. PROMDEM consists of five annual (summer data) gridded elevation maps posted at a 500 m resolution. The dataset covers the marginal zone of the Greenland Ice Sheet, extending 50 km inland. Both products are based the same CryoSat-2 and ICESat-2 for this period. For comparison, PROMDEM was averaged from its native resolution to the JPL 1920 m grid. Elevation change rates were then computed for both datasets over the 2019–2023 period. We find a mean difference of  $10 \pm 91 \text{ cm a}^{-1}$  (JPL mi-

nus PROMDEM), excluding all rates exceeding  $\pm 5 \text{ m a}^{-1}$ . Much of the difference can be attributed to methods used for interpolation and difference in temporal resolution. PROMDEM uses spatial kriging while we use spatial kriging with the addition of an elevation and velocity dependent background model. Determining which dataset is more accurate is challenging, as we lack external data, such as from ATM, to compare over this period.

To estimate mass change, we examine three regions of interest (ROIs) (seen in Table 3): (1) the continental ice sheet, (2) peripheral glaciers and (3) individual drainage basins (Fig. 1) by computing a linear trend for each ROI and period. For the continental ice sheet, we find an overall loss of  $-162 \pm 17 \text{ Gt a}^{-1}$  over the 1992–2023 period. Losses are concentrated in the main outlet glaciers in Greenland, such as the Jakobshavn, Helheim, N79 and Kangerlussuaq glaciers, and in coastal areas by the Denmark Strait on the Blossville coast (Basin 3) and in the North-West between the city of Upernavik and Pituffik Space Base by Baffin Bay (Basin 8). These same regions have also experienced accelerations in rates of ice discharge except for the Jakobshavn Glacier which slowed due to recent ocean cooling (Khazendar et al., 2019), which can be seen in the Fig. 4 panel 2017–2021. The first decade of the record (1992–2001) the ice sheet gained volume at rate of  $+51 \pm 68 \text{ Gt a}^{-1}$ . The ice sheet then began rapidly losing volume in 2004, leading to an extreme rate of volume loss for the second decade of  $-303 \pm 48 \text{ Gt a}^{-1}$ . The mass loss was particularly large over the 2007–2011 period (Fig. 5). In the last decade of the record (2012–2022) there rate of loss slowed to  $-124 \pm 39 \text{ Gt a}^{-1}$ , a rate roughly 60% less negative than the proceeding decade (Figs. 4–5) modulated by the slowdown of some outlet glaciers due to ocean cooling (Khazendar et al., 2019) and positive Surface Mass Balance (SMB) anomaly as seen in Figs. S2 and S3.

Large difference in volume change rates can be observed at the basin scale. The general pattern depicts one of less mass loss in the North increasing southwards, with higher rates of loss in the West compared to the East. Basin 2 is the only region that experienced minimal change in volume over the three decades of observation ( $1 \pm 4 \text{ Gt a}^{-1}$ ). All basins show a relative stable or positive rates of volume change in the first decade of the record. Nearly all Basins entered a regime of volume loss initiated around 2004, except for Basin 6 where the onset of rapid volume loss was delayed until summer of 2009. Most eastern basins experienced a reduction in their rates of loss after 2012 (Basins 2–4). This is also true for the two most Southern Western Basins (5 and 6). Several years (1995, 2012 and 2019) experienced pronounced rates of volume loss instigated by warm summers that produced anomalously high rates of melt water runoff (see SMB anomaly in Fig. S3).

The peripheral glaciers show an overall volume loss of  $-23 \pm 5 \text{ Gt a}^{-1}$  for the period 1992–2023 (Fig. 5), with annual rates modulated with changes in SMB (see Fig. S3). Between 1992–2002 there was relatively little change in pe-

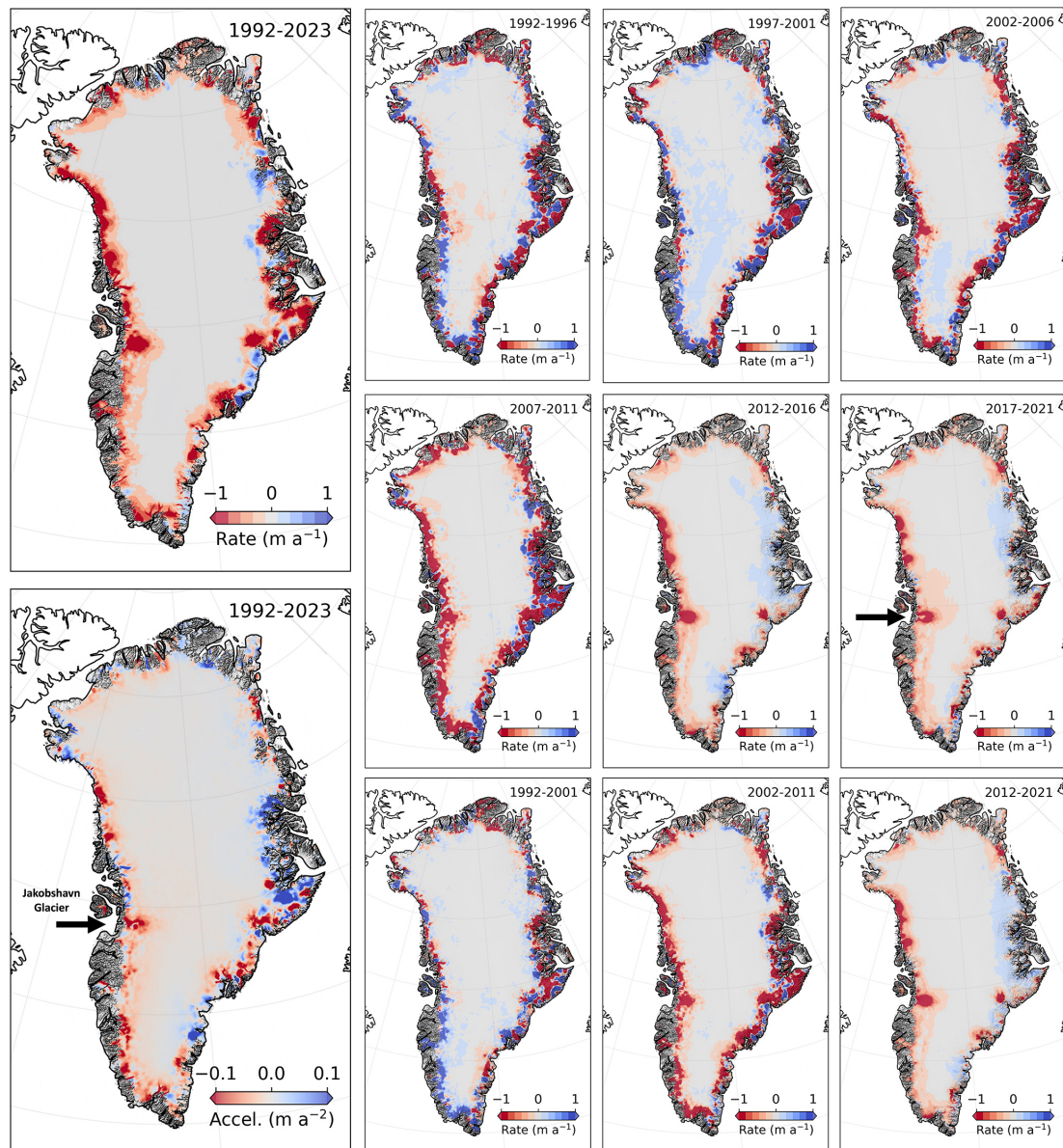


**Figure 4.** Greenland ice elevation change rates and acceleration from our synthesis of multi-mission altimetry for the 3 decades spanning 1992 to 2023. Decadal rates of elevation change are generally positive over the first decade (1992–2001), extremely negative in the second decade (2002–2011), and moderately negative in the third decade (2012–2021). A slowdown of Jakobshavn glacier, due to lower ocean temperatures at its front (Khazendar et al., 2019), can be seen for period 2017–2021 and in the map of acceleration (indicated on the maps with arrows).

ripheral glacier volume, with losses beginning around 2003. Greenland’s peripheral glaciers have not been studied with the same intensity as the continental ice sheet due to challenges associated with sampling and the accuracy of retrievals (similar for altimetry, gravity and input-output methods). However, a few studies have focused on these glaciers over different time intervals; Khan et al. (2022) computed a total loss of  $-27 \pm 6 \text{ Gt a}^{-1}$  from ICESat over the period 2003–2009 and  $-42 \pm 6 \text{ Gt a}^{-1}$  for ICESat-2 over the period 2018–2021. This is almost 40 % less than our esti-

mate of  $-48 \pm 19 \text{ Gt a}^{-1}$  over the ICESat period, but with a stated larger error. However, over the ICESat-2 period our result of  $-31 \pm 19 \text{ Gt a}^{-1}$  but agrees within our stated error. The estimate from this study also aligns with the values obtained by Gardner et al. (2013) of  $-38 \pm 7 \text{ Gt a}^{-1}$  over the period 2003–2009, but are larger than Bolch et al. (2013) of  $-28 \pm 11 \text{ Gt a}^{-1}$  compared to our  $-40 \pm 22 \text{ Gt a}^{-1}$  for the period October 2003 to March 2008. Further comparisons with estimates generated from high-resolution DEM differencing yielded estimates in line with this study. Hugonnet et

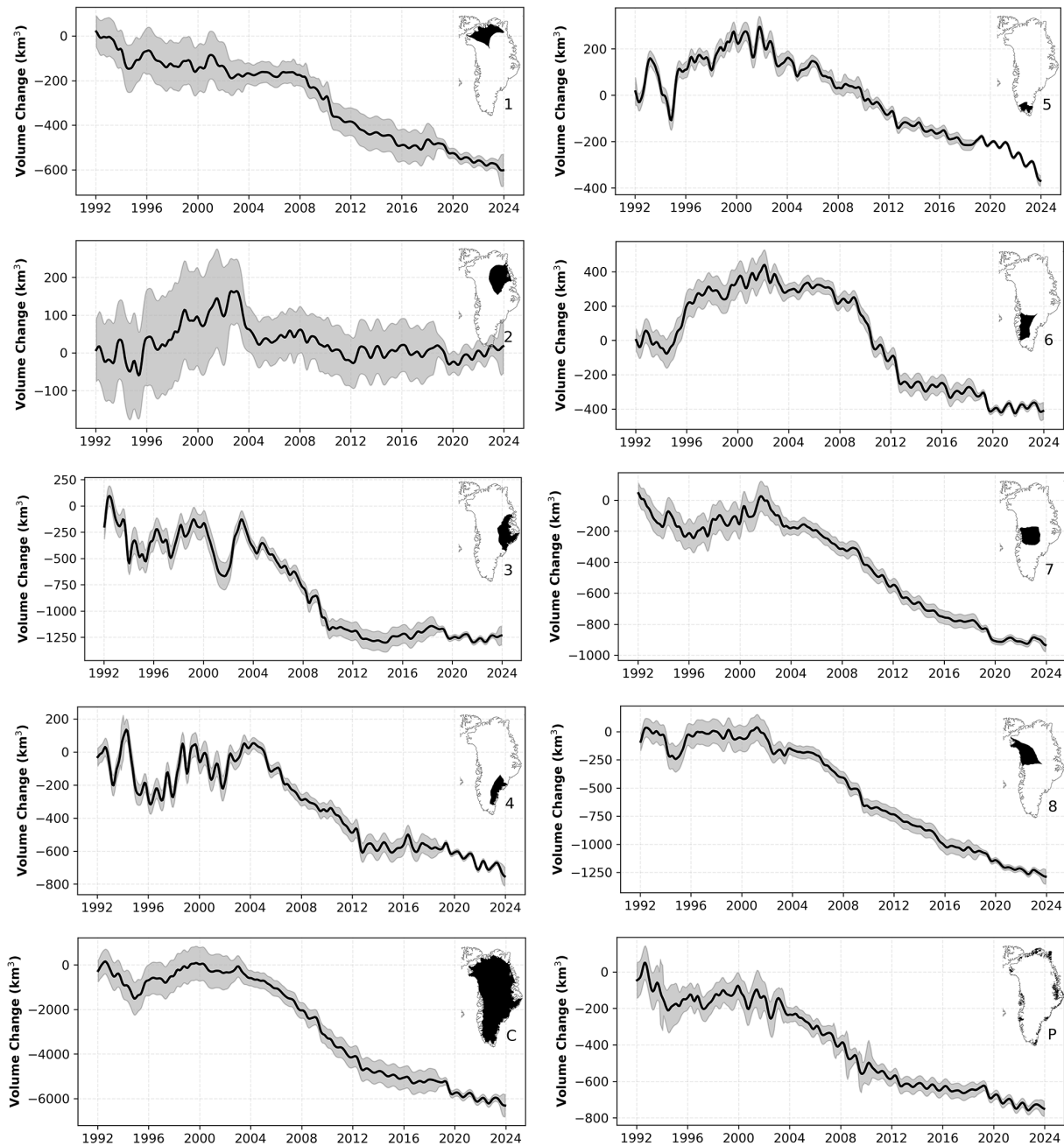


**Figure 5.** Time series of glacier volume anomaly for the continental ice sheet, eight ice sheet drainage basins and peripheral glaciers for the period 1992–2023. Errors are shown with grey shading. Significant improvements in the errors can be seen with the introduction of ICESat-2 data starting in 2018.

al. (2021) estimated a total mass loss of  $-36 \pm 6 \text{ Gt a}^{-1}$  for Greenland’s peripheral glaciers over the 2000–2019 period aligning well with our estimate of  $-29 \pm 6 \text{ Gt a}^{-1}$ . Further, a comparison with modelled results from peripheral glaciers (Schlegel et al., 2016) over the time period of 2003–2012 provided an estimate of  $-37 \pm 25 \text{ Gt a}^{-1}$ . This aligns well with the estimate from this study of  $-43 \pm 13 \text{ Gt a}^{-1}$  over the same period. However, our estimate of  $-25 \pm 5 \text{ Gt a}^{-1}$

for peripheral glaciers during the 2000–2023 period is lower than the community estimate from the “Glacier Mass Balance Intercomparison Exercise” (GlaMBIE), which is  $-35.1 \pm 7.1 \text{ Gt a}^{-1}$  (The GlaMBIE Team et al., 2025).

We further compare our result to those obtained from satellite gravimetry (GRACE and GRACE-FO). For the period 2002 to 2023 gravimetry yields an ice sheet plus peripheral glacier mass change rate of  $-267 \pm 20 \text{ Gt a}^{-1}$  (Wiese et al.,

2019; Watkins et al., 2015). For this comparison the total extent of the periphery was used as GRACE missions can't distinguish between peripheral or continental glaciers. Combining the results for the peripheral glaciers ( $-24 \pm 5 \text{ Gt a}^{-1}$ ) and the continental ice sheet ( $-222 \pm 20 \text{ Gt a}^{-1}$ ) over the same period yields an estimate of  $-246 \pm 23 \text{ Gt a}^{-1}$ , which aligns with the gravity-only estimate.

## 6 Discussion

Our ice sheet altimetry synthesis methodology closely follows that of Nilsson et al. (2022) with a notable enhancement of a new background model. Use of a background model was previously integrated into Nilsson et al. (2022), but failed to yield improved results. In this iteration, significant effort was dedicated to refining background model. Various approaches were explored, and promising results emerged when the overall search radius was expanded to approximately 150 km, effectively accommodating velocity and hypsometric gradients within the data. This augmentation proved beneficial in capturing correlated trends while preserving local behavior at smaller scales. Improvements to the background model help to better capture the elevation change dependence on glacier dynamics via velocity, and to more accurately capture elevation change dependence on elevation that is associated with surface mass balance gradients. The hypsometric component within the background model is of particular importance for peripheral glaciers, compensating for issues related to data quality and coverage over high-relief terrain. Use of elevation to guide the interpolation of elevation change data has been widely employed in the study of glaciers (Gardner et al., 2011; Moholdt et al., 2010, 2012; Nuth et al., 2010) and can be credited with the close agreement observed in this study with several other studies investigating Greenland's peripheral glaciers (Bolch et al., 2013; Gardner et al., 2013; Hugonnet et al., 2021; Khan et al., 2022; Schlegel et al., 2016). We believe the difference in our estimated magnitude of mass loss over the 2003–2009 period, compared to the estimates Bolch et al. (2013), Gardner et al. (2013) and Khan et al. (2022), is attributed to improved data availability and coverage from the Envisat mission included in the study. Although the data is of lower quality, it improves both the spatial and hypsometric coverage below the equilibrium-line altitude during this period, compared to ICESat alone. This is especially true in the southern parts of Greenland, where ICESat tracks diverge and have less coverage. This improvement was supported by an area-hypsometry analysis, which showed more coverage for Envisat at lower elevations ( $< 1000 \text{ m}$ ). The improvement in long term elevation change rates with the inclusion of velocity in the background model is evident in Fig. S1, which illustrates a reduction in overall bias between the datasets derived from our model and those from airborne laser altimetry. Improvements in the background model have enabled us to extend the

record of peripheral glacier elevation changes. However, we posit that further refinement may be achievable by incorporating a more sophisticated version of our Gaussian process scheme. The empirical selection of the 150 km search radius or 3000 closest data points was aimed at capturing correlated gradients while also preserving local behaviors. Nonetheless, we maintain that further enhancements may be attainable through the incorporation of additional external data and more robust gaussian process approach. It is important to emphasize that a background model that utilizes a “remove-and-restore” approach is not novel, as it has been widely employed in geodesy for decades (Moritz, 1978). Further needed enhancement would be the improvement of the slope correction algorithms currently used. This is especially important for the older pulse-limited mission, is still one of the largest error sources in altimetry, but work has been ongoing to improve upon this in newer products such as FDR4ALT. Which will be used in later reprocessing efforts or at least with similar algorithms.

One significant contribution of our new product is the inclusion of peripheral glaciers. To our knowledge, our product is the first to provide estimates of long-term elevation change of these glaciers at the spatial and temporal resolution provided here. The estimates derived from these products demonstrate strong alignment with findings from various studies conducted over different time spans (Bolch et al., 2013; Gardner et al., 2013; Hugonnet et al., 2021; Khan et al., 2022; The GlaMBIE Team et al., 2025). Despite their relatively small area (roughly 4 % of Greenland's ice cover – Khan et al., 2022), peripheral glaciers are found to contribute roughly 12 % of the total ice loss from Greenland over the last three decades. Their inclusion enables a more accurate comparison between altimetry-derived estimates of mass change and those obtained through gravity measurements. The current resolution of GRACE/-FO, on the order of 300 km, poses challenges to isolate peripheral glacier mass change from the ice sheet mass change (Otosaka et al., 2023). Consequently, GRACE/-FO is only able to measure the combined peripheral plus ice sheet mass change. We find good agreement between our Greenland-wide estimate of glacier mass change with those derived from GRACE over the period 2002–2023. This alignment underscores the importance of integrating peripheral glaciers into assessments of Greenland's mass change.

Modeled FAC stands as one of the most critical components for accurately estimating the mass balance of ice sheets, yet it has persistently remained one of the largest sources of error. Over the past few years, the scientific modeling community has made significant advancements in developing a variety of new models aimed at reducing this uncertainty. In this study, two such models have been employed to generate mass loss estimates and explore the relative uncertainty by quantifying model spread. Incorporating several of these models should provide a better understanding of the potential errors in model output. Therefore, this study adopts

**Table 3.** Rates of glacier mass change for Greenland Ice Sheet, its basins and peripheral glaciers over the period of 1992–2023 for various epoch.

Regions (Gt a <sup>-1</sup> )	1992–2001 (Gt a <sup>-1</sup> )	2002–2011 (Gt a <sup>-1</sup> )	2012–2021 (Gt a <sup>-1</sup> )	1992–2023 (Gt a <sup>-1</sup> )	2002–2023 (Gt a <sup>-1</sup> )	2003–2009 (Gt a <sup>-1</sup> )	2000–2023 (Gt a <sup>-1</sup> )	2003–2012 (km <sup>2</sup> )	Area
Basin 1	-8 ± 14	-13 ± 9	-8 ± 8	-11 ± 3	-14 ± 4	-5 ± 13	-13 ± 4	-19 ± 9	351 970
Basin 2	14 ± 14	-8 ± 9	-1 ± 8	1 ± 4	-2 ± 4	-7 ± 13	-2 ± 4	-6 ± 9	510 942
Basin 3	-18 ± 18	-92 ± 14	-4 ± 10	-36 ± 5	-41 ± 6	-102 ± 19	-40 ± 5	-98 ± 13	320 960
Basin 4	-3 ± 20	-37 ± 12	-14 ± 9	-19 ± 5	-27 ± 5	-42 ± 17	-26 ± 5	-42 ± 11	165 505
Basin 5	24 ± 10	-21 ± 8	-12 ± 4	-13 ± 3	-19 ± 3	-15 ± 12	-20 ± 3	-21 ± 8	55 554
Basin 6	42 ± 16	-32 ± 10	-19 ± 7	-18 ± 4	-35 ± 4	-12 ± 15	-33 ± 4	-41 ± 10	290 993
Basin 7	-1 ± 15	-42 ± 11	-28 ± 6	-27 ± 4	-36 ± 4	-33 ± 16	-36 ± 4	-43 ± 10	407 473
Basin 8	1 ± 19	-59 ± 13	-40 ± 9	-38 ± 5	-48 ± 5	-59 ± 18	-48 ± 5	-64 ± 12	423 025
Periphery	-5 ± 21	-41 ± 13	-10 ± 6	-23 ± 5	-24 ± 5	-48 ± 19	-25 ± 5	-43 ± 13	87 836
Continental	51 ± 68	-303 ± 48	-124 ± 39	-160 ± 17	-222 ± 20	-273 ± 66	-218 ± 20	-333 ± 45	1 714 172

an agnostic approach, refraining from favoring one model over the other, under the belief that averaging multiple estimates will yield a more accurate result. This limited comparison reveals that even employing just the ensemble mean can yield satisfactory results. However, it is strongly recommended to conduct further analysis on how surface melt is incorporated into these models, given the different forcing and model physics employed in GEMB-FDM and GSFC-FDM as an example. This is evident in Figs. S4 and S5, which highlight large spatial differences in the estimated FAC rates, as well as temporal divergence, particularly around 2005 when surface melt becomes more prevalent.

The long-term record of Greenland glacier elevation change provided here is the most detailed record currently available. It depicts large variability in elevation change rates that are controlled by ocean-ice interaction and changes in SMB (Hanna et al., 2008; Khazendar et al., 2019; Wang et al., 2023). One interesting finding is the increase in mass of the GrIS in the first decade of the record. This mass increase is consistent with neutral to positive SMB anomalies after the 1995 melt event (Fig. S3) and drop in FAC seen in both products (Fig. S4). Previous studies have either considered this time period stable or showing a negative mass balance (Mouginot et al., 2019; Otosaka et al., 2023; Simonsen et al., 2021). This might be related to the temporal resolution these previous studies have used on the order of several years with large windows for aggregating data to reduce noise. Applying such large windows might have the impact of spreading 1995 melt event to nearby years or removing it depending on the method used. In Otosaka et al. (2023) the 1995 melt event can be seen in the input-output method in Fig. 1 but not in the the final Fig. 4 after generating the cumulative time series of ice sheet mass change by integration. Another interesting finding is that the well-documented slowdown of the front of the Jakobshavn glacier (Khazendar et al., 2019) is well resolved in our product, providing strong evidence of the capability of this updated processing approach to capture these kinds of localized phenom-

ena. Finally our long-term estimate for the continental ice sheet of  $-162 \pm 17 \text{ Gt a}^{-1}$  fits well with the results from the latest “Ice sheet Mass Balance Inter-comparison Exercise” (IMBIE) of  $-169 \pm 9 \text{ Gt a}^{-1}$  (Otosaka et al., 2023). Our results for the 2003–2023 period,  $-218 \pm 21 \text{ Gt a}^{-1}$ , are consistent with Khan et al. (2025), who report  $-217 \pm 16 \text{ Gt a}^{-1}$ , further indicating a convergence of mass-loss estimates for Greenland.

## 7 Code and data availability

Data can be found in Nilsson and Gardner (2024) (<https://doi.org/10.5067/ICFV17DKHZJV>). The code and algorithm used to generate the product are part of the “Cryosphere Altimetry Processing Toolkit” (captopoolkit) and can be found here <https://github.com/nasa-jpl/captopoolkit> (last access: 29 November 2025) and at <https://doi.org/10.5281/zenodo.3665784> (Nilsson et al., 2020).

## 8 Conclusion

Our altimetry synthesis reveals a consistent pattern of surface elevation change rates across the Greenland Ice Sheet and peripheral glaciers, which aligns well with findings from previous studies. By integrating a background model that is guided by velocity and elevation, we manage to achieve higher spatial resolution, particularly in regions experiencing pronounced dynamic thinning. This advancement is crucial, as it allows for the preservation of small-scale and highly localized signals that were previously smoothed out by more traditional interpolation algorithms. Moreover, our background model effectively addresses spatial sampling biases inherent to radar satellite altimeters, enhancing the accuracy of our derived elevation change rates. The accuracy of independent missions varies, with older missions exhibiting higher noise levels compared to more recent ones. Notably, significant differences exist between radar and laser-derived

surface elevations, with laser altimetry outperforming radar across all slopes. While our interpolation algorithm demonstrates overall improved accuracy compared to ordinary optimal interpolation, regional variations persist, particularly in areas of rapid change such as outlet glaciers. On a broader scale, our analysis of long-term volume changes reveals an overall loss of mass for both the continental ice sheet and peripheral glaciers. Specifically, we estimate a combined (ice sheet plus peripheral glaciers) mass loss of  $-183 \pm 18 \text{ Gt a}^{-1}$  over the period 1992–2023. These findings are consistent with previous studies and highlight the ongoing impact of climate change on Greenland's ice mass change. Furthermore, our results demonstrate the importance of accounting for changes in firn air content when estimating mass balance, as the choice of firn model can significantly affect mass balance estimates. In summary, our study contributes to a deeper understanding of Greenland's response to a changing climate and underscores the critical role of satellite altimetry in monitoring long-term changes in ice mass. Moving forward, continued research and refinement of modelling techniques will be essential for further improving estimates of ice sheet and glacier mass change and their contribution to sea level change.

**Supplement.** The supplement related to this article is available online at <https://doi.org/10.5194/essd-18-1729-2026-supplement>.

**Author contributions.** JN and ASG conceptualized the study. JN conducted the analysis, wrote most of the main text, and made all figures. JN and ASG contributed to conceptualization and algorithm development. All authors contributed to the writing and editing of the manuscript.

**Competing interests.** The contact author has declared that neither of the authors has any competing interests.

**Disclaimer.** Publisher's note: Copernicus Publications remains neutral with regard to jurisdictional claims made in the text, published maps, institutional affiliations, or any other geographical representation in this paper. The authors bear the ultimate responsibility for providing appropriate place names. Views expressed in the text are those of the authors and do not necessarily reflect the views of the publisher.

**Acknowledgements.** The authors were supported by the ITS\_LIVE project awarded through NASA MEaSUREs program, and the NASA Cryosphere program through participation in the ICESat-2 science team. We thank the NASA and the European Space Agency (ESA) for distributing their radar altimetry data. The research described in this paper was carried out at the Jet Propulsion Laboratory, California Institute of Technology, under a contract with NASA.

**Financial support.** This research was supported by the Jet Propulsion Laboratory through NASA MEaSUREs and the NASA Cryosphere Science Program, as well as through an agreement with the National Aeronautics and Space Administration. Additional support for the research was provided in part by the Swedish National Space Agency (Rymdstyrelsen).

The publication of this article was funded by the Swedish Research Council, Forte, Formas, and Vinnova.

**Review statement.** This paper was edited by Katrin Lindbäck and reviewed by William Colgan, Rene Forsberg, and Veit Helm.

## References

- Anon: RA-2 Geophysical Data Record, <https://doi.org/10.5270/EN1-ajb696a>, 2018.
- Arthern, R. J., Wingham, D. J., and Ridout, A. L.: Controls on ERS altimeter measurements over ice sheets: Footprint-scale topography, backscatter fluctuations, and the dependence of microwave penetration depth on satellite orientation, *J. Geophys. Res.*, 106, 33471–33484, <https://doi.org/10.1029/2001JD000498>, 2001.
- Bamber, J. L.: Ice sheet altimeter processing scheme, *International Journal of Remote Sensing*, 15, 925–938, <https://doi.org/10.1080/01431169408954125>, 1994.
- Bolch, T., Sandberg Sørensen, L., Simonsen, S. B., Mölg, N., Machguth, H., Rastner, P., and Paul, F.: Mass loss of Greenland's glaciers and ice caps 2003–2008 revealed from ICESat laser altimetry data, *Geophysical Research Letters*, 40, 875–881, <https://doi.org/10.1002/grl.50270>, 2013.
- Borsa, A. A., Fricker, H. A., and Brunt, K. M.: A Terrestrial Validation of ICESat Elevation Measurements and Implications for Global Reanalyses, *IEEE Trans. Geosci. Remote Sensing*, 57, 6946–6959, <https://doi.org/10.1109/TGRS.2019.2909739>, 2019.
- Brenner, A. C., Blndschadler, R. A., Thomas, R. H., and Zwally, H. J.: Slope-induced errors in radar altimetry over continental ice sheets, *J. Geophys. Res.*, 88, 1617–1623, <https://doi.org/10.1029/JC088iC03p01617>, 1983.
- Brockley, D. J., Baker, S., Femenias, P., Martinez, B., Massmann, F.-H., Otten, M., Paul, F., Picard, B., Prandi, P., Roca, M., Rudenko, S., Scharroo, R., and Visser, P.: REAPER: Reprocessing 12 Years of ERS-1 and ERS-2 Altimeters and Microwave Radiometer Data, *IEEE Trans. Geosci. Remote Sensing*, 55, 5506–5514, <https://doi.org/10.1109/TGRS.2017.2709343>, 2017.
- Cleveland, W. S.: Robust Locally Weighted Regression and Smoothing Scatterplots, *J. Am. Stat. Assoc.*, 74, 829–836, <https://doi.org/10.1080/01621459.1979.10481038>, 1979.
- Davis, C. H. and Ferguson, A. C.: Elevation change of the Antarctic ice sheet, 1995–2000, from ERS-2 satellite radar altimetry, *IEEE Trans. Geosci. Remote Sensing*, 42, 2437–2445, <https://doi.org/10.1109/TGRS.2004.836789>, 2004.
- Flament, T. and Rémy, F.: Dynamic thinning of Antarctic glaciers from along-track repeat radar altimetry, *J. Glaciol.*, 58, 830–840, <https://doi.org/10.3189/2012JoG11J118>, 2012.
- Gardner, A. S., Moholdt, G., Wouters, B., Wolken, G. J., Burgess, D. O., Sharp, M. J., Cogley, J. G., Braun, C., and Labine, C.: Sharply increased mass loss from glaciers and ice caps

- in the Canadian Arctic Archipelago, *Nature*, 473, 357–360, <https://doi.org/10.1038/nature10089>, 2011.
- Gardner, A. S., Moholdt, G., Cogley, J. G., Wouters, B., Arendt, A. A., Wahr, J., Berthier, E., Hock, R., Pfeffer, W. T., Kaser, G., Ligtenberg, S. R. M., Bolch, T., Sharp, M. J., Hagen, J. O., Van Den Broeke, M. R., and Paul, F.: A Reconciled Estimate of Glacier Contributions to Sea Level Rise: 2003 to 2009, *Science*, 340, 852–857, <https://doi.org/10.1126/science.1234532>, 2013.
- Gardner, A. S., Schlegel, N.-J., and Larour, E.: Glacier Energy and Mass Balance (GEMB): a model of firn processes for cryosphere research, *Geosci. Model Dev.*, 16, 2277–2302, <https://doi.org/10.5194/gmd-16-2277-2023>, 2023.
- Gray, L., Burgess, D., Copland, L., Dunse, T., Langley, K., and Moholdt, G.: A revised calibration of the interferometric mode of the CryoSat-2 radar altimeter improves ice height and height change measurements in western Greenland, *The Cryosphere*, 11, 1041–1058, <https://doi.org/10.5194/tc-11-1041-2017>, 2017.
- Hanna, E., Huybrechts, P., Steffen, K., Cappelen, J., Huff, R., Shuman, C., Irvine-Fynn, T., Wise, S., and Griffiths, M.: Increased Runoff from Melt from the Greenland Ice Sheet: A Response to Global Warming, *Journal of Climate*, 21, 331–341, <https://doi.org/10.1175/2007JCLI1964.1>, 2008.
- Helm, V., Dehghanpour, A., Hänsch, R., Loebel, E., Horwath, M., and Humbert, A.: AWI-ICENet1: a convolutional neural network retracker for ice altimetry, *The Cryosphere*, 18, 3933–3970, <https://doi.org/10.5194/tc-18-3933-2024>, 2024.
- Houghton, J.: Mass Balance of the Cryosphere: Observations and Modelling of Contemporary and Future Changes, 1st edn., edited by: Bamber, J. L. and Payne, A. J., Cambridge University Press, <https://doi.org/10.1017/CBO9780511535659>, 2004.
- Howat, I. M., Negrete, A., and Smith, B. E.: The Greenland Ice Mapping Project (GIMP) land classification and surface elevation data sets, *The Cryosphere*, 8, 1509–1518, <https://doi.org/10.5194/tc-8-1509-2014>, 2014.
- Hugonnet, R., McNabb, R., Berthier, E., Menounos, B., Nuth, C., Girod, L., Farinotti, D., Huss, M., Dussaillant, I., Brun, F., and Käab, A.: Accelerated global glacier mass loss in the early twenty-first century, *Nature*, 592, 726–731, <https://doi.org/10.1038/s41586-021-03436-z>, 2021.
- Hurkmans, R. T. W. L., Bamber, J. L., Sørensen, L. S., Joughin, I. R., Davis, C. H., and Krabill, W. B.: Spatiotemporal interpolation of elevation changes derived from satellite altimetry for Jakobshavn Isbræ, Greenland, *J. Geophys. Res.*, 117, 2011JF002072, <https://doi.org/10.1029/2011JF002072>, 2012.
- Khan, S. A., Colgan, W., Neumann, T. A., Van Den Broeke, M. R., Brunt, K. M., Noël, B., Bamber, J. L., Hassan, J., and Bjørk, A. A.: Accelerating Ice Loss From Peripheral Glaciers in North Greenland, *Geophysical Research Letters*, 49, e2022GL098915, <https://doi.org/10.1029/2022GL098915>, 2022.
- Khan, S. A., Seroussi, H., Morlighem, M., Colgan, W., Helm, V., Cheng, G., Berg, D., Barletta, V. R., Larsen, N. K., Kochtitzky, W., van den Broeke, M., Kjær, K. H., Aschwanden, A., Noël, B., Box, J. E., MacGregor, J. A., Fausto, R. S., Mankoff, K. D., Howat, I. M., Onizsk, K., Fahrner, D., Løkkegaard, A., Lippert, E. Y. H., Brätner, A., and Hassan, J.: Smoothed monthly Greenland ice sheet elevation changes during 2003–2023, *Earth Syst. Sci. Data*, 17, 3047–3071, <https://doi.org/10.5194/essd-17-3047-2025>, 2025.
- Khazendar, A., Fenty, I. G., Carroll, D., Gardner, A., Lee, C. M., Fukumori, I., Wang, O., Zhang, H., Seroussi, H., Moller, D., Noël, B. P. Y., Van Den Broeke, M. R., Dinardo, S., and Willis, J.: Interruption of two decades of Jakobshavn Isbrae acceleration and thinning as regional ocean cools, *Nat. Geosci.*, 12, 277–283, <https://doi.org/10.1038/s41561-019-0329-3>, 2019.
- Khvorostovsky, K. S.: Merging and Analysis of Elevation Time Series Over Greenland Ice Sheet From Satellite Radar Altimetry, *IEEE Trans. Geosci. Remote Sensing*, 50, 23–36, <https://doi.org/10.1109/TGRS.2011.2160071>, 2012.
- Levinsen, J. F., Simonsen, S. B., Sørensen, L. S., and Forsberg, R.: The Impact of DEM Resolution on Relocating Radar Altimetry Data Over Ice Sheets, *IEEE J. Sel. Top. Appl. Earth Observations Remote Sensing*, 9, 3158–3163, <https://doi.org/10.1109/JSTARS.2016.2587684>, 2016.
- MacGregor, J. A., Boisvert, L. N., Medley, B., Petty, A. A., Harbeck, J. P., Bell, R. E., Blair, J. B., Blanchard-Wrigglesworth, E., Buckley, E. M., Christoffersen, M. S., Cochran, J. R., Csathó, B. M., De Marco, E. L., Dominguez, R. T., Fahnestock, M. A., Farrell, S. L., Gogineni, S. P., Greenbaum, J. S., Hansen, C. M., Hofton, M. A., Holt, J. W., Jezek, K. C., Koenig, L. S., Kurtz, N. T., Kwok, R., Larsen, C. F., Leuschen, C. J., Locke, C. D., Manizade, S. S., Martin, S., Neumann, T. A., Nowicki, S. M. J., Paden, J. D., Richter-Menge, J. A., Rignot, E. J., Rodríguez-Morales, F., Siegfried, M. R., Smith, B. E., Sonntag, J. G., Studinger, M., Tinto, K. J., Truffer, M., Wagner, T. P., Woods, J. E., Young, D. A., and Yungel, J. K.: The Scientific Legacy of NASA's Operation IceBridge, *Reviews of Geophysics*, 59, e2020RG000712, <https://doi.org/10.1029/2020RG000712>, 2021.
- McMillan, M., Leeson, A., Shepherd, A., Briggs, K., Armitage, T. W. K., Hogg, A., Kuipers Munneke, P., Van Den Broeke, M., Noël, B., Van De Berg, W. J., Ligtenberg, S., Horwath, M., Groh, A., Muir, A., and Gilbert, L.: A high-resolution record of Greenland mass balance, *Geophysical Research Letters*, 43, 7002–7010, <https://doi.org/10.1002/2016GL069666>, 2016.
- Medley, B., Neumann, T. A., Zwally, H. J., Smith, B. E., and Stevens, C. M.: Simulations of firn processes over the Greenland and Antarctic ice sheets: 1980–2021, *The Cryosphere*, 16, 3971–4011, <https://doi.org/10.5194/tc-16-3971-2022>, 2022.
- Moholdt, G., Nuth, C., Hagen, J. O., and Kohler, J.: Recent elevation changes of Svalbard glaciers derived from ICESat laser altimetry, *Remote Sensing of Environment*, 114, 2756–2767, <https://doi.org/10.1016/j.rse.2010.06.008>, 2010.
- Moholdt, G., Wouters, B., and Gardner, A. S.: Recent mass changes of glaciers in the Russian High Arctic, *Geophysical Research Letters*, 39, 2012GL051466, <https://doi.org/10.1029/2012GL051466>, 2012.
- Moritz, H.: Least-squares collocation, *Reviews of Geophysics*, 16, 421–430, <https://doi.org/10.1029/RG016i003p00421>, 1978.
- Mouginot, J., Rignot, E., Bjørk, A. A., Van Den Broeke, M., Millan, R., Morlighem, M., Noël, B., Scheuchl, B., and Wood, M.: Forty-six years of Greenland Ice Sheet mass balance from 1972 to 2018, *Proc. Natl. Acad. Sci. U.S.A.*, 116, 9239–9244, <https://doi.org/10.1073/pnas.1904242116>, 2019.
- Nilsson, J. and Gardner, A.: MEASURE ITS\_LIVE Greenland Ice Sheet Elevation and Mass Change, Version 1, ITS\_LIVE [data set], <https://doi.org/10.5067/ICFV17DKHZJV>, 2024.

- Nilsson, J., Vallelonga, P., Simonsen, S. B., Sørensen, L. S., Forsberg, R., Dahl-Jensen, D., Hirabayashi, M., Goto-Azuma, K., Hvidberg, C. S., Kjær, H. A., and Satow, K.: Greenland 2012 melt event effects on CryoSat-2 radar altimetry, *Geophysical Research Letters*, 42, 3919–3926, <https://doi.org/10.1002/2015GL063296>, 2015.
- Nilsson, J., Gardner, A., Sandberg Sørensen, L., and Forsberg, R.: Improved retrieval of land ice topography from CryoSat-2 data and its impact for volume-change estimation of the Greenland Ice Sheet, *The Cryosphere*, 10, 2953–2969, <https://doi.org/10.5194/tc-10-2953-2016>, 2016.
- Nilsson, J., Paolo, F., and Gardner, A.: fspaolo/captoolkit: First release, Zenodo [code], <https://doi.org/10.5281/zenodo.3665784>, 2020.
- Nilsson, J., Gardner, A. S., and Paolo, F. S.: Elevation change of the Antarctic Ice Sheet: 1985 to 2020, *Earth Syst. Sci. Data*, 14, 3573–3598, <https://doi.org/10.5194/essd-14-3573-2022>, 2022.
- Nuth, C., Moholdt, G., Kohler, J., Hagen, J. O., and Kääh, A.: Svalbard glacier elevation changes and contribution to sea level rise, *J. Geophys. Res.*, 115, 2008JF001223, <https://doi.org/10.1029/2008JF001223>, 2010.
- Otosaka, I. N., Shepherd, A., Ivins, E. R., Schlegel, N.-J., Amory, C., van den Broeke, M. R., Horwath, M., Joughin, I., King, M. D., Krinner, G., Nowicki, S., Payne, A. J., Rignot, E., Scambos, T., Simon, K. M., Smith, B. E., Sørensen, L. S., Velicogna, I., Whitehouse, P. L., A. G., Agosta, C., Ahlstrøm, A. P., Blazquez, A., Colgan, W., Engdahl, M. E., Fettweis, X., Forsberg, R., Gallée, H., Gardner, A., Gilbert, L., Gourmelen, N., Groh, A., Gunter, B. C., Harig, C., Helm, V., Khan, S. A., Kittel, C., Konrad, H., Langen, P. L., Lecavalier, B. S., Liang, C.-C., Loomis, B. D., McMillan, M., Melini, D., Mernild, S. H., Mottram, R., Mouginot, J., Nilsson, J., Noël, B., Pattle, M. E., Peltier, W. R., Pie, N., Roca, M., Sasgen, I., Save, H. V., Seo, K.-W., Scheuchl, B., Schrama, E. J. O., Schröder, L., Simonsen, S. B., Slater, T., Spada, G., Sutterley, T. C., Vishwakarma, B. D., van Wessem, J. M., Wiese, D., van der Wal, W., and Wouters, B.: Mass balance of the Greenland and Antarctic ice sheets from 1992 to 2020, *Earth Syst. Sci. Data*, 15, 1597–1616, <https://doi.org/10.5194/essd-15-1597-2023>, 2023.
- Paolo, F. S., Fricker, H. A., and Padman, L.: Constructing improved decadal records of Antarctic ice shelf height change from multiple satellite radar altimeters, *Remote Sensing of Environment*, 177, 192–205, <https://doi.org/10.1016/j.rse.2016.01.026>, 2016.
- Paolo, F. S., Gardner, A. S., Greene, C. A., Nilsson, J., Schodlok, M. P., Schlegel, N.-J., and Fricker, H. A.: Widespread slowdown in thinning rates of West Antarctic ice shelves, *The Cryosphere*, 17, 3409–3433, <https://doi.org/10.5194/tc-17-3409-2023>, 2023.
- Porter, C., Howat, I., Noh, M.-J., Husby, E., Khuvis, S., Danish, E., Tomko, K., Gardiner, J., Negrete, A., Yadav, B., Klassen, J., Kelleher, C., Cloutier, M., Bakker, J., Enos, J., Arnold, G., Bauer, G., Morin, P., and Polar Geospatial Center: ArcticDEM – Mosaics, Version 4.1 (1.0), Harvard Dataverse [data set], <https://doi.org/10.7910/DVN/3VDC4W>, 2023.
- RGI Consortium: Randolph Glacier Inventory – A Dataset of Global Glacier Outlines, (NSIDC-0770, Version 6), Boulder, Colorado USA, National Snow and Ice Data Center [data set], <https://doi.org/10.7265/4m1f-gd79>, 2017.
- Roemer, S., Legrésy, B., Horwath, M., and Dietrich, R.: Refined analysis of radar altimetry data applied to the region of the subglacial Lake Vostok/Antarctica, *Remote Sensing of Environment*, 106, 269–284, <https://doi.org/10.1016/j.rse.2006.02.026>, 2007.
- Schlegel, N.-J., Wiese, D. N., Larour, E. Y., Watkins, M. M., Box, J. E., Fettweis, X., and van den Broeke, M. R.: Application of GRACE to the assessment of model-based estimates of monthly Greenland Ice Sheet mass balance (2003–2012), *The Cryosphere*, 10, 1965–1989, <https://doi.org/10.5194/tc-10-1965-2016>, 2016.
- Schröder, L., Richter, A., Fedorov, D. V., Eberlein, L., Brovkvov, E. V., Popov, S. V., Knöfel, C., Horwath, M., Dietrich, R., Matveev, A. Y., Scheinert, M., and Lukin, V. V.: Validation of satellite altimetry by kinematic GNSS in central East Antarctica, *The Cryosphere*, 11, 1111–1130, <https://doi.org/10.5194/tc-11-1111-2017>, 2017.
- Schröder, L., Horwath, M., Dietrich, R., Helm, V., van den Broeke, M. R., and Ligtenberg, S. R. M.: Four decades of Antarctic surface elevation changes from multi-mission satellite altimetry, *The Cryosphere*, 13, 427–449, <https://doi.org/10.5194/tc-13-427-2019>, 2019.
- Simonsen, S. B. and Sørensen, L. S.: Implications of changing scattering properties on Greenland ice sheet volume change from Cryosat-2 altimetry, *Remote Sensing of Environment*, 190, 207–216, <https://doi.org/10.1016/j.rse.2016.12.012>, 2017.
- Simonsen, S. B., Barletta, V. R., Colgan, W. T., and Sørensen, L. S.: Greenland Ice Sheet Mass Balance (1992–2020) From Calibrated Radar Altimetry, *Geophysical Research Letters*, 48, e2020GL091216, <https://doi.org/10.1029/2020GL091216>, 2021.
- Smith, B., Fricker, H. A., Gardner, A. S., Medley, B., Nilsson, J., Paolo, F. S., Holschuh, N., Adusumilli, S., Brunt, K., Csatho, B., Harbeck, K., Markus, T., Neumann, T., Siegfried, M. R., and Zwally, H. J.: Pervasive ice sheet mass loss reflects competing ocean and atmosphere processes, *Science*, 368, 1239–1242, <https://doi.org/10.1126/science.aaz5845>, 2020.
- Smith, B., Adusumilli, S., Csathó, B. M., Felikson, D., Fricker, H. A., Gardner, A. S., Holschuh, N., Lee, J., Nilsson, J., Paolo, F., Siegfried, M. R., Sutterley, T., and the ICESat-2 Science Team: ATLAS/ICESat-2 L3A Land Ice Height, Version 6, Boulder, Colorado USA, NASA National Snow and Ice Data Center Distributed Active Archive Center [data set], <https://doi.org/10.5067/ATLAS/ATL06.006>, 2023.
- The GLAMBIE Team, Zemp, M., Jakob, L., Dussaillant, I., Nussbaumer, S. U., Gourmelen, N., Dubber, S., A. G., Abdullahi, S., Andreassen, L. M., Berthier, E., Bhattacharya, A., Blazquez, A., Boehm Vock, L. F., Bolch, T., Box, J., Braun, M. H., Brun, F., Cicero, E., Colgan, W., Eckert, N., Farinotti, D., Florentine, C., Floricioiu, D., Gardner, A., Harig, C., Hassan, J., Hugonnet, R., Huss, M., Jóhannesson, T., Liang, C.-C. A., Ke, C.-Q., Khan, S. A., King, O., Kneib, M., Krieger, L., Maussion, F., Mattea, E., McNabb, R., Menounos, B., Miles, E., Moholdt, G., Nilsson, J., Pálsson, F., Pfeffer, J., Piermattei, L., Plummer, S., Richter, A., Sasgen, I., Schuster, L., Seehaas, T., Shen, X., Sommer, C., Sutterley, T., Treichler, D., Velicogna, I., Wouters, B., Zekollari, H., and Zheng, W.: Community estimate of global glacier mass changes from 2000 to 2023, *Nature*, 639, 382–388, <https://doi.org/10.1038/s41586-024-08545-z>, 2025.
- The IMBIE team: Mass balance of the Antarctic Ice Sheet from 1992 to 2017, *Nature*, 558, 219–222, <https://doi.org/10.1038/s41586-018-0179-y>, 2018.

- Wang, Z., Zhang, B., Yao, Y., and Zhang, W.: GRACE and mass budget method reveal decelerated ice loss in east Greenland in the past decade, *Remote Sensing of Environment*, 286, 113450, <https://doi.org/10.1016/j.rse.2023.113450>, 2023.
- Watkins, M. M., Wiese, D. N., Yuan, D., Boening, C., and Landerer, F. W.: Improved methods for observing Earth's time variable mass distribution with GRACE using spherical cap mascons, *JGR Solid Earth*, 120, 2648–2671, <https://doi.org/10.1002/2014JB011547>, 2015.
- Wiese, D. N., Yuan, D.-N., Boening, C., Landerer, F. W., and Watkins, M. M.: JPL GRACE and GRACE-FO Mascon Ocean, Ice, and Hydrology Equivalent Water Height CRI Filtered. Ver. RL06Mv02. PO.DAAC [data set], CA, USA, <https://doi.org/10.5067/TEMSC-3JC62>, 2019.
- Wingham, D. J., Ridout, A. J., Scharroo, R., Arthern, R. J., and Shum, C. K.: Antarctic Elevation Change from 1992 to 1996, *Science*, 282, 456–458, <https://doi.org/10.1126/science.282.5388.456>, 1998.
- Winstrup, M.: PRODEM: Annual summer DEMs of the marginal areas of the Greenland Ice Sheet, GEUS Dataverse V10 [data set], <https://doi.org/10.22008/FK2/52WWHG>, 2023.
- Winstrup, M., Rannal, H., Hillerup Larsen, S., Simonsen, S. B., Mankoff, K. D., Fausto, R. S., and Sandberg Sørensen, L.: PRODEM: an annual series of summer DEMs (2019 through 2022) of the marginal areas of the Greenland Ice Sheet, *Earth Syst. Sci. Data*, 16, 5405–5428, <https://doi.org/10.5194/essd-16-5405-2024>, 2024.
- Wouters, B., Martín-Español, A., Helm, V., Flament, T., Van Wessem, J. M., Ligtenberg, S. R. M., Van Den Broeke, M. R., and Bamber, J. L.: Dynamic thinning of glaciers on the Southern Antarctic Peninsula, *Science*, 348, 899–903, <https://doi.org/10.1126/science.aaa5727>, 2015.
- Zwally, H. J., Giovinetto, M. B., Li, J., Cornejo, H. G., Beckley, M. A., Brenner, A. C., Saba, J. L., and Yi, D.: Mass changes of the Greenland and Antarctic ice sheets and shelves and contributions to sea-level rise: 1992–2002, *J. Glaciol.*, 51, 509–527, <https://doi.org/10.3189/172756505781829007>, 2005.
- Zwally, H. J., Giovinetto, M. B., Beckley, M. A., and Saba, J. L.: *Antarctic and Greenland Drainage Systems*, 2012.